Hydrogen-Assisted Crack Propagation in Austenitic Stainless Steel Fusion Welds

B.P. SOMERDAY, M. DADFARNIA, D.K. BALCH, K.A. NIBUR, C.H. CADDEN, and P. SOFRONIS

The objective of this study was to characterize hydrogen-assisted crack propagation in gas-tungsten arc (GTA) welds of the nitrogen-strengthened, austenitic stainless steel 21Cr-6Ni-9Mn (21-6-9), using fracture mechanics methods. The fracture initiation toughness and crack growth resistance curves were measured using fracture mechanics specimens that were thermally precharged with 230 wppm (1.3 at. pct) hydrogen. The fracture initiation toughness and slope of the crack growth resistance curve for the hydrogen-precharged weld were reduced by as much as 60 and 90 pct, respectively, relative to the noncharged weld. A physical model for hydrogen-assisted crack propagation in the welds was formulated from microscopy evidence and finite-element modeling. Hydrogen-assisted crack propagation proceeded by a sequence of microcrack formation at the weld ferrite, intense shear deformation in the ligaments separating microcracks, and then fracture of the ligaments. One salient role of hydrogen in the crack propagation process was promoting microcrack formation at austenite/ferrite interfaces and within the ferrite. In addition, hydrogen may have facilitated intense shear deformation in the ligaments separating microcracks. The intense shear deformation could be related to the development of a nonuniform distribution of hydrogen trapped at dislocations between microcracks, which in turn created a gradient in the local flow stress.

I. INTRODUCTION

AUSTENITIC stainless steels are well suited as structural materials in hydrogen environments, because this alloy class is one of the most resistant to hydrogen-assisted fracture.[1–3] Although the hydrogen-assisted fracture of austenitic steels has been extensively studied,[3,4] few efforts have focused on welds. Fusion welds in austenitic steels are generally designed to solidify as primary ferrite, which results in the retention of a small amount of δ ferrite following the solid-state transformations that occur during cooling.[5] Because ferritic steels can be highly susceptible to hydrogen-assisted fracture,[1–3] the presence of ferrite in austenitic stainless steel welds raises concerns about the fracture resistance of welds in hydrogen environments.

Studies of the hydrogen-assisted fracture in austenitic stainless steel welds are limited[6–11] and almost none used fracture mechanics methods to quantify fracture resistance and assess fracture mechanisms. Efforts to characterize hydrogen-assisted fracture in austenitic steel welds using tensile tests showed that tensile ductility was degraded and weld ferrite served as the preferred sites for fracture.[6–8] Hydrogen promoted the separation of the austenite/ferrite interface and fracture of the ferrite itself, although the predominant mechanism was not consistent among the studies and likely depended on variables such as the hydrogen concentration and volume fraction of ferrite. Although such tensile fracture studies provide some insight into hydrogen-assisted fracture, the results have limited use in understanding crack extension in structures exposed to hydrogen environments. Fracture toughness data are needed to assess the susceptibility of welds to hydrogen-assisted crack extension. In addition, the hydrostatic stress field ahead of a crack could activate mechanisms of hydrogen-assisted fracture that are not accessible in the uniaxial stress field of a tensile specimen.

The objective of this study was to characterize hydrogen-assisted crack propagation in gas-tungsten arc (GTA) welds of the nitrogen-strengthened, austenitic stainless steel 21Cr-6Ni-9Mn (21-6-9) using fracture mechanics methods. The fracture initiation toughness and crack growth resistance curves were measured using fracture mechanics specimens that were thermally precharged in hydrogen gas. Mechanisms of hydrogen-assisted crack propagation in the welds were identified from the examination of fracture surfaces and fracture profiles using electron microscopy. A physical model for hydrogen-assisted crack propagation in the welds was formulated from microscopy evidence and finite-element modeling.

B.P. SOMERDAY, Principal Member of Technical Staff, D.K. BALCH, Senior Member of Technical Staff, and K.A. NIBUR, Postdoctoral Research Associate, are with Sandia National Laboratories, Livermore, CA 94550. Contact e-mail: bpsomer@sandia.gov M. DADFARNIA, Postdoctoral Research Associate, and P. SOFRONIS, Professor, are with the Department of Mechanical Engineering, University of Illinois at Urbana–Champaign, Urbana, IL 61801. C.H. CADDEN, formerly Manager with Sandia National Laboratories, is deceased.
Manuscript submitted July 22, 2008.
Article published online August 8, 2009

II. EXPERIMENTAL PROCEDURES

The base metal product form of the 21-6-9 austenitic stainless steel was a rectangular bar with a cross section 75 × 75 mm in size, in which this final square cross section was achieved by forging. Tests conducted on transverse-oriented uniaxial tensile specimens (gage section 19 mm in length and 4 mm in diameter) indicated that the bar had a true yield stress of 485 MPa (0.2 pct offset) and a true ultimate tensile stress of 1135 MPa. The average composition of the bar was measured by a commercial vendor (Anamet, Inc., Hayward, CA) and is provided in Table I. Also included in Table I is the composition reported in the alloy certification documentation for the bar.

A groove having a cross section shaped like a tapered "U" was machined along the longitudinal direction in a section removed from the rectangular bar. The groove was subsequently filled with 21-6-9 filler wire using 32 GTA weld passes; the welding parameters are summarized in Table II and a macrograph of the finished weld is shown in Figure 1. The filler wire composition was designed to promote primary ferrite solidification by increasing the concentrations of the ferrite stabilizers (e.g., Cr) and decreasing the concentrations of the austenite stabilizers (e.g., Ni and N) relative to the base metal. The average composition of the weld fusion zone was measured at the same time as the base metal and is reported in Table I. This weld, consisting of 21-6-9 base metal and 21-6-9 filler metal, is referred to as 21-6-9/21-6-9.

Crack propagation in the weld fusion zone was studied using compact tension (CT) specimens, which were designed following ASTM Standard E1737-96.[12] The CT specimens had a width of 26.5 mm, a gross thickness of 6.0 mm, and a net thickness of 4.6 mm between the side grooves. The precrack starter notch was oriented normal to the longitudinal axis of the rectangular bar, and the tip of the notch was located near the base of the weld (Figure 1). The CT specimens were fatigue precracked in air to a final crack length-to-width ratio between 0.48 and 0.50 under a final maximum stress-intensity factor of approximately 30 MPa·$\sqrt{m}$. The fatigue precrack was grown in a direction parallel to the weld solidification direction and extended approximately 1 to 2 mm into the weld fusion zone along the weld centerline.

The fatigue-precracked CT specimens removed from welds were tested in the as-welded condition and after thermal charging in hydrogen gas. The hydrogen-precharged specimens were exposed to 99.99 pct hydrogen gas at 138 MPa and 573 K for 29 days. The charging time and temperature assured that the hydrogen concentration at the specimen midthickness was at least 90 pct of the equilibrium hydrogen concentration at the surface. Following hydrogen precharging, hydrogen egress from the CT specimens was minimized by maintaining the specimens at a temperature less than 250 K at all times, except during mechanical testing.
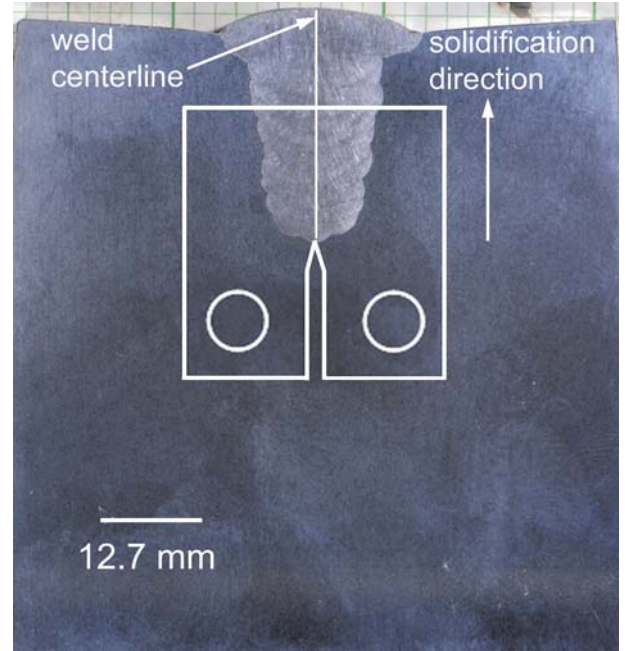

Fig. 1—Macrograph of the cross section of the finished 21-6-9/21-6-9 GTA weld. Centerline and solidification direction of the weld are indicated on the image. Outline of the CT specimen on the macrograph shows the location and orientation of the specimen relative to the weld.

Table II. Fabrication Parameters for 21-6-9/21-6-9 GTA Welds

Weld Parameter	Value
Current (A)	250
Voltage (V)	11
Travel speed (cm/min)	7.6
Maximum interpass temperature (K)	533
Argon shielding gas flow rate (Nm^3/h)	0.4
Filler wire feed rate (cm/min)	76

Table I. Measured Compositions (Weight Percent) of Base Metal and Weld Fusion Zone*

Material	Cr	Ni	Mn	Mo	N	C	Si	P	S	Cr$_{eq}$**	Ni$_{eq}$**
Weld	19.54	6.81	9.39	0.10	0.19	0.030	0.25	<0.005	<0.002	19.6	11.7
Base metal	19.07	6.96	9.78	0.17	0.26	0.018	0.52	0.045	0.005	19.2	12.9
Base metal†	19.27	6.98	9.68	0.35	0.28	0.013	0.53	0.025	0.001	19.6	13.0

*Composition balances are Fe.
**Cr$_{eq}$ = Cr + Mo + 0.7Nb; Ni$_{eq}$ = Ni + 35C + 20N + 0.25Cu.[15]
†Composition from alloy certification documentation.

The hydrogen content in the weld fusion zone was measured from material that was removed from the back face of a CT specimen after mechanical testing. The average hydrogen content was 230 wppm (1.3 at. pct), as measured using an inert-gas fusion instrument at a commercial laboratory (ATI Wah Chang, Albany, OR). This hydrogen content is consistent with that calculated from the thermal precharging parameters and the solubility of 21-6-9 base materials.[13]

Fracture mechanics tests were conducted on the CT specimens using procedures in ASTM standard E1737-96.[12] All CT specimens were tested in air at room temperature, including the hydrogen-precharged specimens, which were warmed to room temperature prior to testing. The specimens were loaded under actuator displacement control in a servohydraulic test frame, in which the displacement rate was 0.4 mm/min for duplicate tests on both hydrogen-precharged and noncharged specimens. One additional test was conducted on a hydrogen-precharged specimen at a displacement rate of 0.04 mm/min. At these loading rates, the fracture initiation toughness was reached in approximately 3 and 25 minutes, respectively, for the hydrogen-precharged specimens. Crack-opening displacement (COD) was measured with a clip gage located at the load line, and crack extension was continuously monitored using the direct-current potential difference (DCPD) technique operating at a constant current of 1 A. Following testing, the CT specimens were heated at 623 K for 60 minutes to tint the fracture surfaces. The specimens were then broken apart, and the fatigue precrack lengths and total crack lengths were measured from the fracture surfaces. The total crack lengths calculated from the DCPD data were within 10 pct of the total crack lengths measured from the fracture surfaces of hydrogen-precharged specimens. For the noncharged specimens, the difference between calculated and measured total crack lengths was approximately 1 pct. The DCPD-calculated crack lengths were linearly corrected to force the calculated and measured total crack lengths to be equal.

The J-integral crack growth resistance (R) curve was constructed following guidance in ASTM E1737, *e.g.*, the initial linear J vs crack growth increment (Δa) relationship was calculated based on an assumed crack blunting response. The onset of crack extension following blunting was defined using the DCPD data, where the point of crack initiation was identified as the second slope change of the DCPD-*vs*-COD trend. The physical evidence from fracture mechanics testing on stainless steels indicated that the second slope change of the DCPD *vs* COD trend corresponded to crack initiation.[14] The fracture initiation toughness was defined using standardized procedures, *i.e.*, the intersection of the 0.2-mm-offset blunting line with the R curve.

Microstructures, fracture surfaces, and fracture profiles from the welds were examined using a combination of optical microscopy and scanning electron microscopy (SEM). Chemical compositions of phases in the weld fusion zone were determined by energy-dispersive spectroscopy (EDS) in the scanning electron microscope. The ferrite content of the weld fusion zone was measured using a calibrated commercial digital ferrite gage.

III. RESULTS

A. *Microstructure*

The volume fraction of ferrite was measured along the centerline of the 21-6-9/21-6-9 weld fusion zone. The average ferrite number (FN) measured at locations of 2, 6, 10, 14, and 18 mm above the base of the weld was 7.3, 8.7, 6.9, 6.7, and 7.6 ($\pm$0.3 maximum variation from average), respectively. At low values of FN, the FN is approximately equal to the volume fraction of ferrite. The FN range measured for the weld fusion zone is consistent with the FN predicted from the WRC-1992 diagram (*i.e.*, FN $\approx$ 8),[15] given the calculated Cr_{eq} and Ni_{eq} for the weld metal (Table I). No ferrite was detected in the base metal at distances greater than 2 mm from the fusion zone/base metal boundary.

The morphology and distribution of ferrite in the weld fusion zone are revealed from optical microscopy and SEM images. The optical image in Figure 2(a) shows the general morphology of ferrite in the weld. This image is from a position near the weld centerline, and the solidification direction is from the bottom to the top of the image. Based on comparing images such as that in Figure 2(a) with the results for other austenitic stainless steel welds,[5,7] two distinct morphologies of ferrite are identified in the 21-6-9/21-6-9 weld: skeletal ferrite and lathy ferrite (labeled "S" and "L," respectively, in Figure 2(a)). The backscatter electron image in Figure 2(b) reveals more details of the size, shape, and spacing of the ferrite. The Cr_{eq} and Ni_{eq} values calculated for the weld (Table I), coupled with the presence of both skeletal and lathy ferrite as well as the relatively high volume fraction of ferrite, support the expectation that the weld solidified as primary ferrite. In this case, the ferrite is located along former dendrite cores.[5]

B. *Fracture Toughness*

Hydrogen severely reduces the fracture toughness of 21-6-9/21-6-9 welds, as demonstrated from both the fracture initiation toughness as well as the slope of the crack growth resistance curve. The crack growth resistance curves for both hydrogen-precharged and noncharged welds are compared in Figure 3. The data in Figure 3 represent duplicate tests for each condition at 0.4 mm/min displacement rate. The crack growth resistance curves from duplicate tests coincide, and the data illustrate the dramatic effect of hydrogen on the crack propagation resistance of the weld.

The fracture initiation toughness and R curve slope were determined from crack growth resistance curves such as those displayed in Figure 3. Values of the fracture initiation toughness and R curve slope are summarized in Table III for both hydrogen-precharged and noncharged welds. In the noncharged condition, the CT specimens did not meet the size requirements for
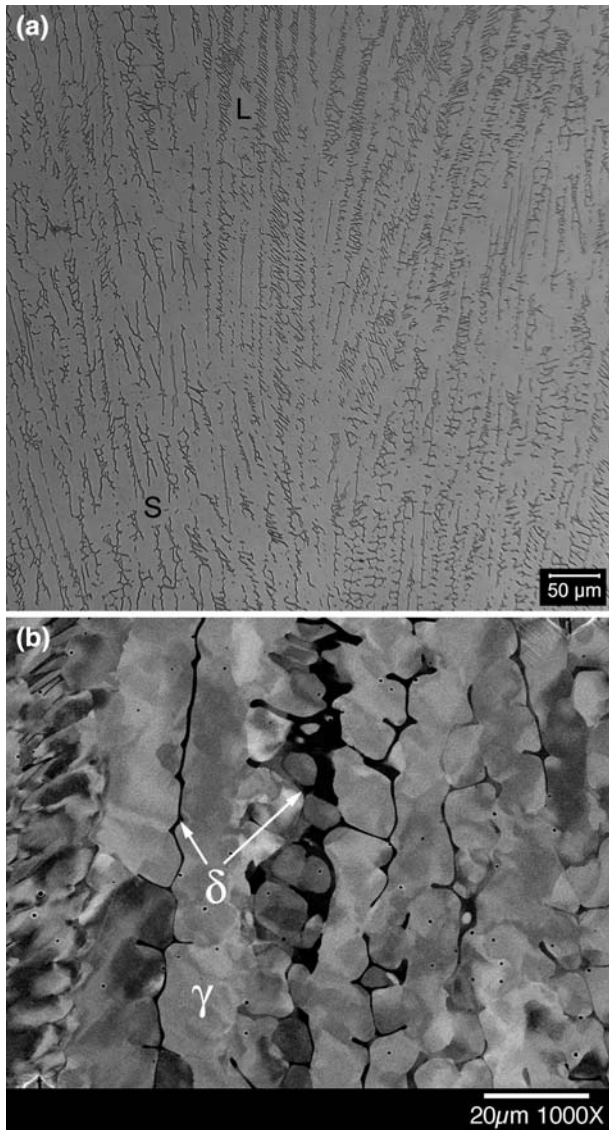
Fig. 2—Microstructure of the fusion zone in the 21-6-9/21-6-9 GTA weld: (a) optical image showing both skeletal (S) and lathy (L) ferrite and (b) high-magnification, backscatter electron image showing details of ferrite (δ) in the austenite (γ) matrix. The imaging areas are at the weld centerline and the solidification direction is from bottom to top in the images.

Fig. 3—J integral (J) vs crack extension (Δa) plots for 21-6-9/21-6-9 GTA welds in the hydrogen-precharged and noncharged conditions. The dashed line is the 0.2-mm offset blunting line.

Table III. Fracture Mechanics Properties for 21-6-9/21-6-9 GTA Welds

Condition	Loading Rate (mm/min)	J (kJ/m^2)	K_J^* (MPa·$\sqrt{\text{m}}$)	$dJ/d\Delta a$** (kJ/m^2/mm)
Noncharged	0.4	$J_Q = 439$	$K_{JQ} = 308$	499
Noncharged	0.4	$J_Q = 444$	$K_{JQ} = 310$	579
H$_2$ charged	0.4	$J_{IH} = 94.8$	$K_{JIH} = 143$	94.9
H$_2$ charged	0.4	$J_{IH} = 96.7$	$K_{JIH} = 145$	103
H$_2$ charged	0.04	$J_{IH} = 77.4$	$K_{JIH} = 129$	65

*Calculated from $K_J = \left(\frac{JE}{1-\nu^2}\right)^{1/2}$, where E and ν are listed in Table IV.
**Measured over 0.5 mm of crack extension immediately following blunting.

plane strain and *J* dominance; thus, the fracture initiation toughness values in Table III are reported as J_Q. In contrast, the lower initiation toughness values for the hydrogen-precharged welds allowed these CT specimens to meet the size requirements. These fracture initiation toughness values are reported as J_{IH} in Table III. Because the stress-intensity factor *K* is a more common fracture mechanics parameter in structural design, the values of the *J*-integral fracture initiation toughness J_Q and J_{IH} were converted to K_{JQ} and K_{JIH}. As shown in Table III, hydrogen reduces the fracture initiation toughness from approximately 310 to 145 MPa·$\sqrt{\text{m}}$, where the latter value represents tests conducted at a displacement rate of 0.4 mm/min. When the displacement rate was lowered to 0.04 mm/min,
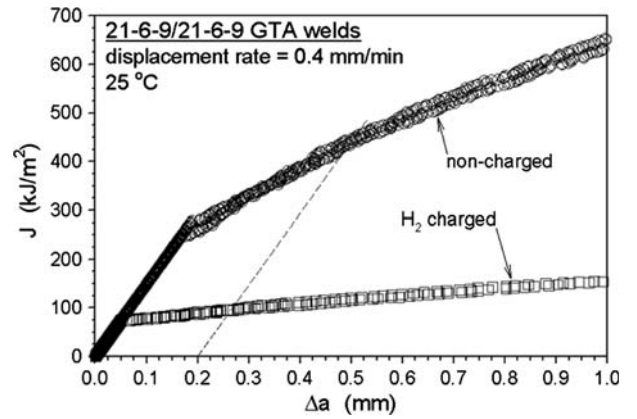
the fracture initiation toughness decreased even further to approximately 130 MPa·$\sqrt{\text{m}}$. These K_{JQ} and K_{JIH} values demonstrate that hydrogen degrades the fracture initiation toughness by as much as 60 pct.

Similar to the fracture initiation toughness, hydrogen reduced the slope of the crack growth resistance curve. Table III shows that values of the *R* curve slope $dJ/d\Delta a$ were approximately 540 and 100 kJ/m^2/mm in the noncharged and hydrogen-precharged conditions, respectively, at a displacement rate of 0.4 mm/min. When the displacement rate was lowered to 0.04 mm/min, hydrogen had a more pronounced effect on the *R* curve slope, *i.e.*, $dJ/d\Delta a$ equaled 65 kJ/m^2/mm.

C. *Fractography*

Hydrogen markedly altered the fracture mode of the 21-6-9/21-6-9 welds. The change in fracture mode is readily apparent from the SEM images of the fracture surfaces, as shown in Figure 4. The fracture surfaces from specimens tested in the noncharged condition (Figure 4(a)) are uniformly covered with dimples, indicating that the fracture mode was microvoid nucleation, growth, and coalescence. In contrast, dimples are a minority feature on the fracture surfaces from
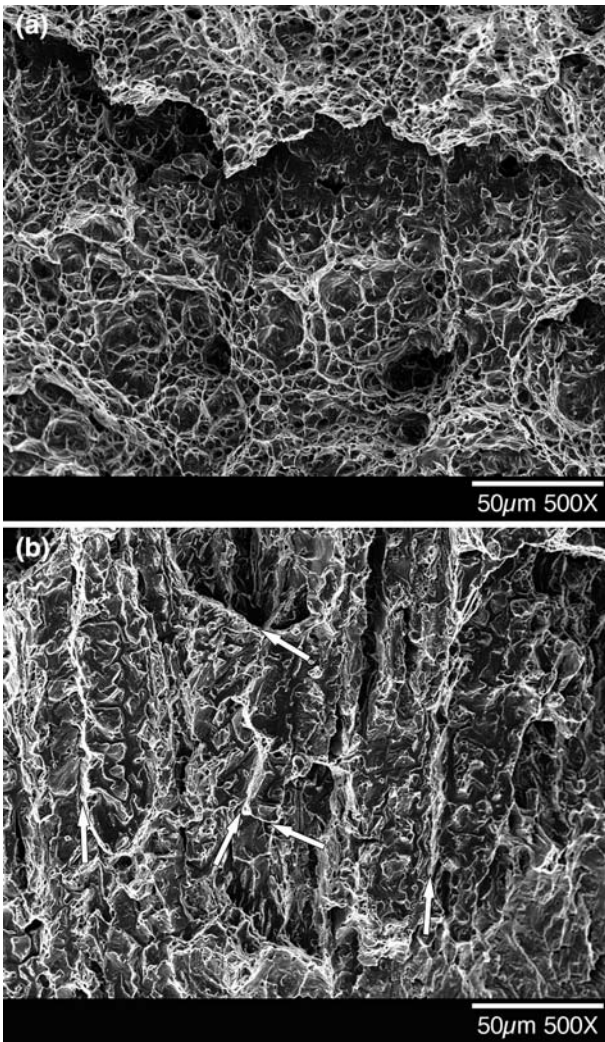
Fig. 4—Secondary electron images of fracture surfaces from (a) noncharged 21-6-9/21-6-9 GTA weld and (b) hydrogen-pre-charged 21-6-9/21-6-9 GTA weld. Each imaging area is adjacent to the fatigue precrack tip, which is located at the bottom of the image. The arrows in (b) indicate steps on the fracture surface where each arrow is oriented parallel to the face of a step.

the hydrogen-precharged welds (Figure 4(b)). The pre-dominant characteristics of these fracture surfaces are features that appear to reflect the weld dendritic microstructure. These features are oriented parallel to the crack propagation direction and the weld solidification direction.

Analysis of the fracture surfaces in the SEM using high-magnification imaging and EDS provides further insight into the hydrogen-assisted fracture mode of the weld. Figure 5 shows two pairs of images, in which each image in a pair represents the same location on matching fracture surfaces from a hydrogen-precharged weld. In Figures 5(a) and (b), EDS spectra from within the regions outlined by dotted lines on both surfaces showed elevated concentrations of Cr but lower concentrations of Ni compared to the areas immediately surrounding these regions. These results indicate that the regions bounded by dotted lines are the ferrite phase,

because this phase is enriched in ferrite stabilizers such as Cr and depleted in austenite stabilizers such as Ni. The presence of ferrite at the same location on opposite fracture surfaces is evidence that cracking proceeded through the ferrite. In other locations, EDS analysis demonstrated that ferrite matched with austenite on opposite fracture surfaces, e.g., Figures 5(c) and (d). These observations indicate that cracking also followed austenite/ferrite interfaces.

Examination of fracture surface profiles provides additional perspectives on the hydrogen-assisted fracture process of the weld. Figure 6 shows backscatter electron images of cross sections through the fracture surfaces from hydrogen-precharged welds. In Figure 6(a), the fracture surface profile is parallel to the direction of crack propagation. This image illustrates that crack propagation was parallel to the aligned dendritic microstructure of the weld and also reveals two important features of the crack propagation process. First, microcracks associated with the ferrite phase formed parallel to the primary fracture plane. Based on evidence from the fracture surfaces (e.g., Figure 5), these microcracks result from separation of the austenite/ferrite interface or from fracture of the ferrite phase itself. The second notable feature from Figure 6(a) is the stepped nature of the fracture surface profile. The fracture surface steps are not only characteristic of the profile parallel to the crack propagation direction but also of the profile transverse to the crack propagation direction (e.g., Figure 6(b)). Imaging of some of these steps at higher magnification reveals evidence for intense deformation in the adjacent material. For example, Figure 6(c) shows a step from the transverse fracture profile in which the adjacent ferrite has been reoriented due to deformation.

The identification of steps from the fracture profiles helps with the interpretation of features on the fracture surfaces, such as those indicated by arrows in Figure 4(b). Using the stereoimaging technique, features such as the ones indicated by arrows in Figure 4(b) were confirmed as steps on the fracture surface. Consistent with observations from the fracture profiles, the faces of these steps are oriented both parallel and transverse to the crack propagation direction.

IV. DISCUSSION

A. Fracture Toughness Measurements

The resistance of the fusion zone in 21-6-9/21-6-9 GTA welds to hydrogen-assisted fracture was measured from hydrogen-precharged CT specimens, in which the fatigue precrack was oriented parallel to the aligned dendritic microstructure of the weld. In this orientation, the weld fusion zone was highly susceptible to hydrogen-assisted fracture, as indicated by the measurements of the fracture initiation toughness and the slope of the crack growth resistance curve. The fracture initiation toughness of the hydrogen-precharged weld K_{JIH} was as low as 40 pct of the initiation toughness of the non-charged weld K_{JQ} (Table III). In addition, the slope of
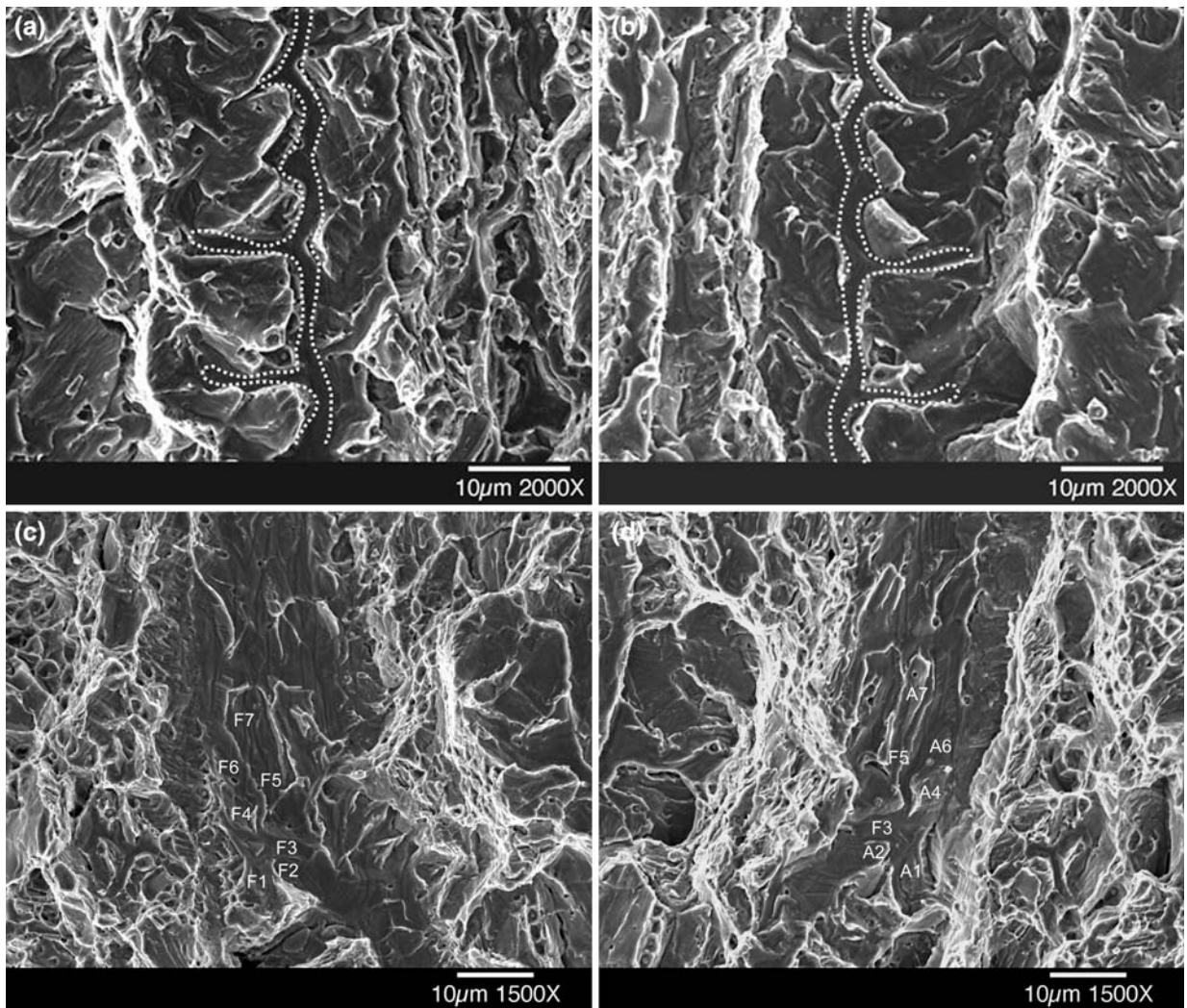
Fig. 5—Secondary electron images of fracture surfaces from the hydrogen-precharged 21-6-9/21-6-9 GTA weld showing matching areas from opposite surfaces. In the matching images (*a*) and (*b*), EDS analysis indicates that the regions bounded by the dotted lines are the ferrite phase. In images (*c*) and (*d*), EDS analysis indicates that matching areas 1, 2, 4, 6, and 7 have austenite (A) on one surface and ferrite (F) on the other; areas 3 and 5 have ferrite on both surfaces.

the *R* curve $dJ/d\Delta a$ of the hydrogen-precharged weld was as low as 10 pct of the value for the noncharged weld (Table III).

The fracture resistance of the 21-6-9/21-6-9 GTA weld was not compared to the fracture resistance of the base metal in this study. However, fracture measurements from the 21-6-9/21-6-9 weld can be compared to the results from other 21-6-9 base metal products. For example, the fracture initiation toughness and slope of the crack growth resistance curve were measured for 21-6-9 forgings using methods similar to those in the current study.[14] The *J*-integral fracture initiation toughness of the forged base metal containing no ferrite was reduced from 1220 kJ/m^2 for the noncharged condition to 240 kJ/m^2 for the hydrogen-precharged condition (230 wppm hydrogen). This 80 pct reduction in fracture initiation toughness is similar to the reduction measured for the 21-6-9/21-6-9 weld, but the absolute value of the fracture initiation toughness is

notably higher for the hydrogen-precharged base metal (240 kJ/m^2) compared to the value for the hydrogen-precharged weld (95 kJ/m^2, Table III). Moreover, the slopes of the crack growth resistance curves follow similar trends, *i.e.*, the value for the hydrogen-precharged base metal (440 kJ/m^2/mm) is considerably higher than the value for the hydrogen-precharged weld (100 kJ/m^2/mm, Table III). These comparisons suggest that GTA welds are more susceptible to hydrogen-assisted fracture than the base metal for 21-6-9.

The hydrogen-assisted fracture resistance of fusion welds in austenitic stainless steels has not been extensively characterized using fracture mechanics methods. In a study similar to the one reported here, Morgan *et al.* measured the crack propagation resistance parallel to the solidification direction in austenitic stainless steel fusion welds containing different volume fractions of ferrite.[9] Two GTA welds from the Morgan *et al.* study had ferrite volume fractions (6 to 8 vol pct) similar to
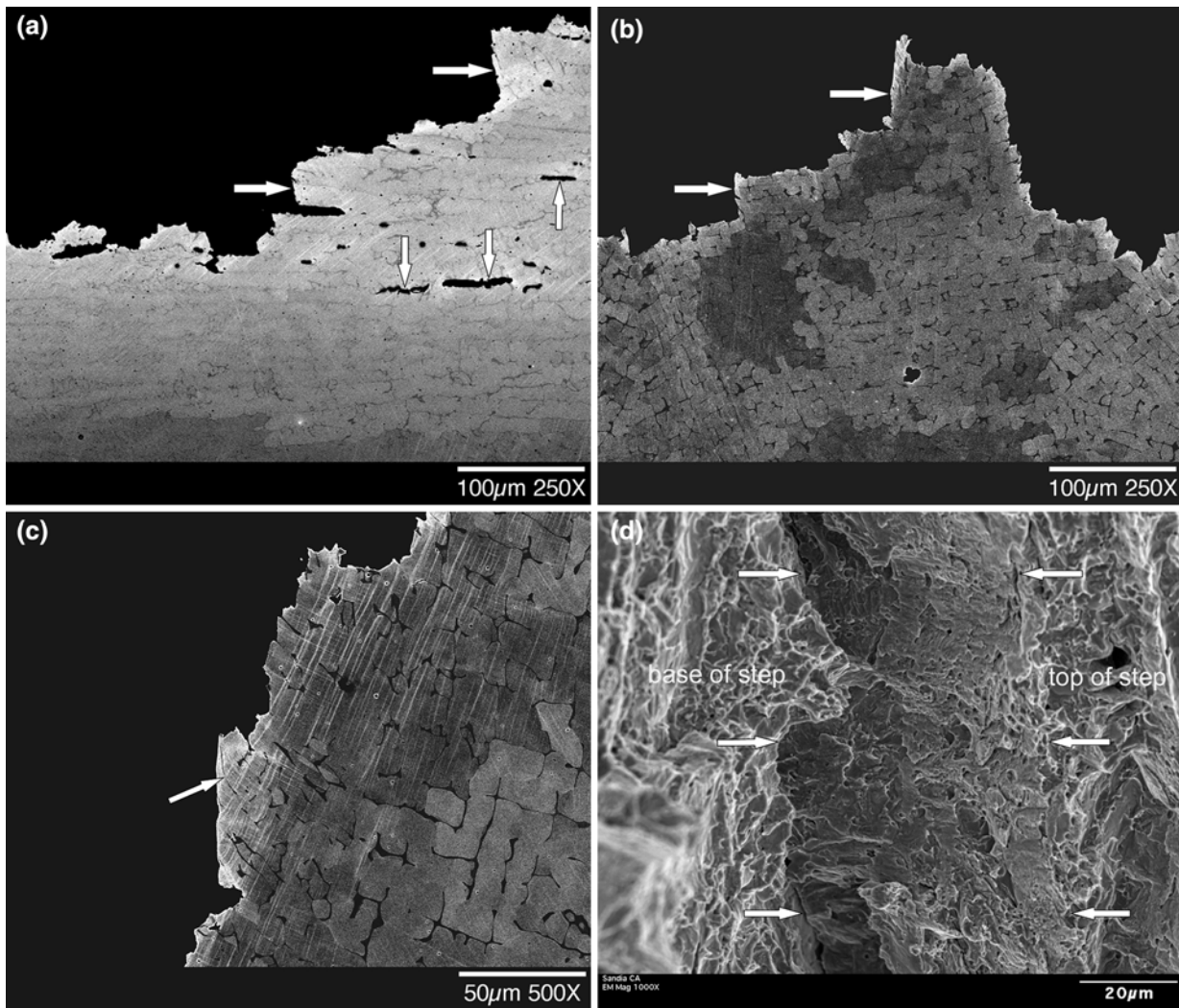
Fig. 6—The backscatter electron images in (*a*), (*b*), and (*c*) show fracture profiles from a hydrogen-precharged 21-6-9/21-6-9 GTA weld. Crack propagation direction is from right to left in (a) and is normal to the page in (b) and (c). Arrows in (a) and (b) indicate microcracks at ferrite or steps on the fracture surface. Arrow in (c) indicates deformed ferrite. The secondary electron image in (*d*) shows a fracture surface tilted at 45 deg to reveal the face of a step similar to those in (b). Crack propagation is from bottom to top in the image. Arrows in (d) indicate the base and top of the step.

the welds in the present work: 21-6-9 base metal with 308L filler wire (21-6-9/308L) and 304L base metal with 308L filler wire (304L/308L). Tests on hydrogen-precharged fracture mechanics specimens from these welds gave *J*-integral fracture initiation toughness values between 114 and 135 kJ/m^2 at a displacement rate of 0.05 mm/min. These initiation toughness values are greater than the initiation toughness measured for the 21-6-9/21-6-9 weld at a displacement rate of 0.04 mm/min (77 kJ/m^2, Table III).

Several variables could account for the lower fracture toughness in 21-6-9/21-6-9 welds compared to 21-6-9/308L and 304L/308L welds: higher constraint in the 21-6-9/21-6-9 fracture mechanics specimen (the fracture mechanics specimen in the Morgan *et al.* study had a gross thickness of only 4.5 mm), higher yield strength in the 21-6-9/21-6-9 weld (21-6-9 filler metal likely leads to higher strength than 308L filler metal due to nitrogen in the former), and a higher hydrogen

content in the 21-6-9/21-6-9 weld. Considering the last variable, the thermal precharging conditions for the welds in the Morgan *et al.* study (35 MPa hydrogen at 623 K) are expected to produce a lower hydrogen content in the 21-6-9/308L and 304L/308L welds compared to the 21-6-9/21-6-9 welds from the current study. This expectation was tested by estimating the hydrogen content of the 21-6-9/308L and 304L/308L welds using solubility data for 300-series stainless steels.[13] Assuming ferrite does not significantly alter the hydrogen content in the fusion zone, consistent with results for the 21-6-9/21-6-9 welds in the present study, the thermal precharging conditions of 35 MPa hydrogen gas and 623 K temperature yield a hydrogen concentration of approximately 70 wppm in the 308L. As expected, this hydrogen content is considerably less than the hydrogen content of the 21-6-9/21-6-9 welds (230 wppm) and could account for the difference in the measured fracture toughness.

B. Fracture Mechanisms

1. Role of weld ferrite

The severe reductions in the fracture toughness of hydrogen-precharged welds (Figure 3 and Table III) are consistent with the striking change in the fracture mode, as illustrated in Figure 4. The microvoid nucleation, growth, and coalescence fracture mode predominates in the noncharged welds, but scant evidence for this fracture mode is found for the hydrogen-precharged welds. Rather, the hydrogen-precharged welds exhibit a fracture mode governed by the dendritic microstructure, in which hydrogen facilitates the separation of austenite/ferrite interfaces and the fracture of the ferrite itself. These crack propagation paths, with respect to the weld ferrite, were conclusively established through matching-pair fractography (e.g., Figure 5).

The mechanisms of hydrogen-assisted fracture involving the weld ferrite can be postulated based on results from other studies. For example, in a duplex stainless steel containing approximately 50 vol pct ferrite and 50 vol pct austenite, hydrogen induced cleavage fracture in the ferrite phase.[16] The cleavage fracture was observed in both tensile specimens and fracture mechanics specimens that were thermally precharged using the same conditions as in the current study, i.e., 138 MPa hydrogen gas at 573 K. In addition, cleavage fracture in ferrite stringers was observed in fracture mechanics specimens from 21-6-9 forgings, in which the crack propagation direction was parallel to the ferrite stringers.[14] These 21-6-9 forgings contained less than 2 vol pct ferrite and were also subjected to the same thermal precharging conditions used in the current study. For both the duplex steel and the 21-6-9 forging, it was concluded that cleavage fracture in the ferrite phase was promoted by hydrogen dissolved in the austenite phase. Localized deformation can develop in the austenite phase as a result of the hydrogen-enhanced localized plasticity mechanism,[17–20] leading to stress concentrations at locations in which deformation bands impinge on austenite/ferrite interfaces. These high local stresses result in a lower remote stress for initiating cleavage cracking in ferrite.

An additional condition that may be required for cleavage fracture in ferrite is high hydrostatic stress. Hydrogen-assisted fracture in thermally precharged tensile specimens from the same 21-6-9 forging referenced earlier did not involve cleavage fracture in the ferrite stringers.[21] Additionally, tensile tests on 21-6-9/21-6-9 welds that were thermally precharged with hydrogen showed evidence of the separation of austenite/ferrite interfaces but not cleavage crack formation in the ferrite.[6,7] In specimens with hydrogen concentrations resulting from thermal precharging, cleavage fracture in the ferrite stringers or weld ferrite was only observed in fracture mechanics specimens, in which high hydrostatic stress develops at the crack tip.

Mechanistic insight into the separation of austenite/ferrite interfaces is provided by other studies of austenitic stainless steel welds. Using the hydrogen microprint technique, elevated hydrogen concentrations were observed at austenite/ferrite interfaces in 304/310, 304/308, and 304/312 welds that were electrolytically precharged with hydrogen.[8] Such elevated hydrogen concentrations create favorable conditions for crack formation at austenite/ferrite interfaces. In addition, it was proposed that alloy composition gradients in the austenite near the ferrite interfaces in welds could lower both the austenite stability and the stacking-fault energy at these locations.[7] Consequently, strain-induced martensite formation and planar slip are promoted and, because these metallurgical features are linked to hydrogen-assisted fracture, the near-interface regions become more susceptible. Local variations in austenite stability and stacking-fault energy were invoked to explain the fracture at austenite/ferrite interfaces in tensile specimens from a range of stainless steel welds, including 21-6-9/21-6-9 welds that were thermally precharged with hydrogen and then strained in air or thermally precharged with hydrogen and then strained in hydrogen gas.[7]

The mechanisms for cleavage fracture in ferrite and interface separation at austenite/ferrite interfaces cited earlier from previous studies are presumed to operate in the 21-6-9/21-6-9 welds from the current study. The metallurgical and environmental conditions associated with cleavage fracture in ferrite stringers from the 21-6-9 forging[14] referenced earlier are particularly germane to the 21-6-9/21-6-9 welds. For example, the 21-6-9 forging and 21-6-9/21-6-9 welds had similar hydrogen concentrations and these two materials are expected to exhibit similar degrees of localized deformation in the austenite phase.

2. Role of intense shear deformation

The formation of microcracks at the weld ferrite is likely the first step in hydrogen-assisted crack propagation. This notion is supported by the image in Figure 6(a), which shows that microcracks initiated at locations away from the primary crack plane but did not propagate. Evidence for how these microcracks link and ultimately lead to crack propagation is provided by the steps on the fracture surface, which are revealed in Figures 4(b) and 6(a) and (b). High-magnification images, such as in Figure 6(c), demonstrate that intense shear deformation developed in the material adjacent to some of these steps.

Based on the fractography results, hydrogen-assisted crack propagation in the welds is postulated to proceed in the following way. As the primary crack tip opens, microcracks form in succession at various locations ahead of the crack tip. Because of the uniform orientation of the weld ferrite, these microcracks are aligned on parallel planes. As the crack tip continues to open, intense shear deformation develops in the ligaments separating microcracks, leading to the fracture of these ligaments and linking of the microcracks. This process of microcrack linking through intense shear deformation and fracture in the ligaments enables crack propagation in orthogonal directions, e.g., along both the longitudinal and transverse directions of the CT specimens.

Although hydrogen has one clear role in the crack propagation process, i.e., inducing microcrack

formation at the weld ferrite, it may also have a role in facilitating intense shear deformation in the ligaments separating microcracks. One possibility is that hydrogen participates in an autocatalytic shear localization-void formation process, as described by Hirth.[22,23] Assuming this mechanism operates in the hydrogen-precharged 21-6-9/21-6-9 welds, deformation could start to localize in the ligaments separating the microcracks as the primary crack tip opens. This deformation creates strain incompatibility at second-phase particles, leading to void nucleation. While strain incompatibility creates a driving force for void nucleation, hydrogen can facilitate void nucleation by lowering the cohesive strength of the particle/matrix interface. The presence of voids can then further intensify the shear deformation in the ligament.

Assuming that the shear deformation between microcracks was aggravated by void formation, it was expected that evidence for voids would be found on the faces of the fracture surface steps. Several such steps from a hydrogen-precharged 21-6-9/21-6-9 weld were examined in the scanning electron microscope by tilting the fracture surface 45 deg to expose the faces of the steps. An image illustrating the typical features on the face of these steps is shown in Figure 6(d). This image reveals that dimples are a minority feature on the faces of the steps, suggesting that void formation was not a predominant mechanism for intense shear deformation between microcracks.

One facet of the hydrogen-enhanced localized plasticity mechanism is that hydrogen enhances the mobility of dislocations, which effectively leads to a decrease in the local flow stress.[17,20,24] Such hydrogen-mediated changes in the local flow stress can cause macroscopic shear instability.[25] At issue is whether hydrogen could facilitate shear instability between microcracks in the weld. This issue is addressed in the Section 3 through applying a finite-element model that is formulated based on the physics of hydrogen-enhanced localized plasticity.

3. Modeling of deformation and hydrogen redistribution between microcracks

The domain of analysis for the solution of the initial/boundary-value problem for transient hydrogen transport coupled with material deformation was chosen based on the physical evidence described in Section IV–B. Figure 7(a) shows a schematic of the fracture process zone in front of the main crack, where overlapping microcracks on parallel planes interact under load. The material response between microcracks was simulated in the domain shown in Figure 7(b) under uniaxial plane strain conditions. The width of the domain $L_w = 48\ \mu m$, the height $L_h = 170\ \mu m$, the length of microcracks within the domain $L_c = 30\ \mu m$, and the distance between them $L_d = 30\ \mu m$. The values for the microcrack length and spacing were determined from examination of fracture profiles similar to that in Figure 6(a). The domain was loaded incrementally by Δu_y, while it was constrained ($u_x = 0$) in the x direction (Figure 7(b)). The constraint tension was chosen in order to account for the presence of the elevated
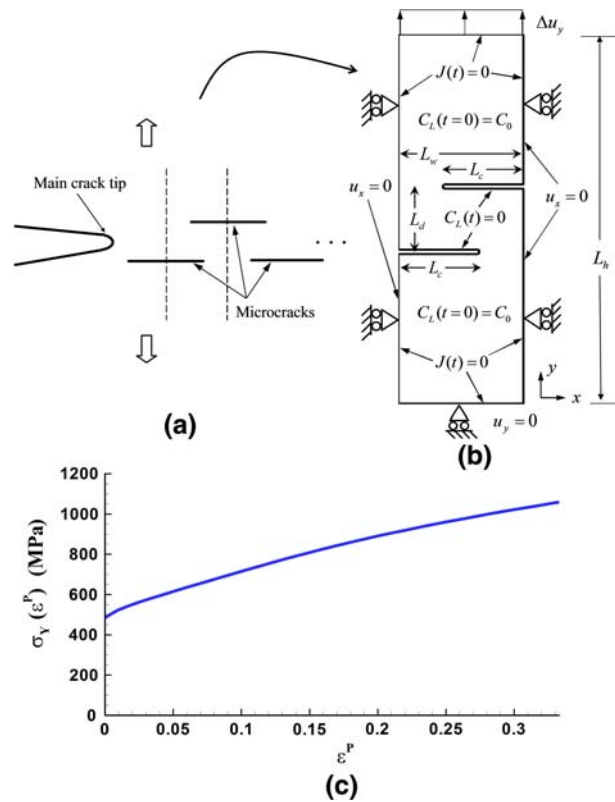

Fig. 7—(a) Schematic of microcracks ahead of the main crack. (b) Description of boundary conditions for the elastoplastic problem and initial and boundary conditions for the diffusion problem near the overlapping microcracks. (c) Stress-plastic strain curve for 21-6-9 base material.

hydrostatic stress environment in the region ahead of the main crack in which the microcracks are forming. Displacement increments were imposed such that the macroscopic strain in the y direction reached 10 pct in 2 minutes, the time at which crack propagation was observed to initiate in the CT specimen of the 21-6-9/21-6-9 weld under a 0.4 mm/min displacement rate. The 10 pct strain represents approximately the plastic strain a material volume experiences in the fracture process zone at distance equal to the crack tip opening displacement ahead of the main crack tip. Throughout the simulation domain and before straining (time $t = 0$), hydrogen was assumed to be uniformly distributed in the lattice at the average concentration measured for the hydrogen-precharged 21-6-9/21-6-9 welds, i.e., $c_0 = 1.3$ at. pct (or $C_0 = 1.1003 \times 10^{27}$ H/m³). In view of the fact that the microcracks were assumed to be periodically located ahead of the main crack, the outer boundary of the domain was assumed impermeable to hydrogen and it was assigned a zero flux boundary condition, $J = 0$. A zero concentration boundary condition was prescribed on the microcrack faces.

The finite-element procedures for the solution of the coupled problems of transient hydrogen diffusion and material elastoplasticity are outlined in work by Sofronis and McMeeking[26] and Liang and Sofronis.[27] Upon straining, hydrogen was modeled to diffuse

through normal interstitial lattice sites (NILS) and become trapped at dislocations that served as reversible traps the density of which increased with plastic straining. The model captures the effect of hydrostatic stress on hydrogen diffusion through NILS.[28] The trapped hydrogen was assumed to always be in equilibrium with the hydrogen at NILS according to Oriani's theory,[29] such that the occupancy of the interstitial lattice sites θ_L and the occupancy of the trapping sites θ_T were related through $\theta_T/(1 - \theta_T) = \theta_L/(1 - \theta_L) K_T$, where $K_T = \exp(E_B/RT)$ represents the equilibrium constant, E_B the trap binding energy, $R = 8.314$ J/mol K, and $T = 298$ K. The hydrogen concentration in trapping sites C_T, measured in hydrogen atoms per unit volume, can be expressed as $C_T = \theta_T \alpha N_T$, where α denotes the number of sites per trap and $N_T = N_T(\varepsilon^p)$ denotes the trap density in the number of traps per unit volume and is a function of the amount of the local plastic strain ε^p. Assuming one trap per atomic plane threaded by a dislocation,[30,31] one finds that the trap density in traps per unit volume is given by $N_T = \sqrt{2}\rho/d$, where d is the lattice parameter and ρ is the dislocation density, which was assumed to increase linearly with plastic strain, that is, $\rho = \rho_0 + \gamma\varepsilon^p$ for $\varepsilon^p \leq 0.5$ and $\rho = $ const. for $\varepsilon^p > 0.5$, $\rho_0 = 10^{10}$ line length/m³, and $\gamma = 2 \times 10^{16}$ line length/m³.[32] Similarly, the hydrogen concentration C_L in NILS, measured in hydrogen atoms per unit volume, can be phrased as $C_L = \theta_L\beta N_L$, where β denotes the number of NILS per solvent atom and N_L denotes the number of solvent atoms per unit volume given by $N_L = N_A/V_M$, with $N_A = 6.0232 \times 10^{23}$ atoms per mole being Avogadro's number and V_M the molar volume of the host lattice.

In agreement with microscopic studies of the effect of hydrogen on dislocation mobility enhancement,[17,20,24] the flow stress of the material was considered[25] to vary with the amount of hydrogen trapped at dislocations: $\sigma_Y(\varepsilon^p, c_T) = \sigma_0[c_T(\xi - 1) + 1]F(\varepsilon^p)$, where σ_0 is the yield stress in the absence of hydrogen, $\xi \leq 1$ is a parameter describing the extent of softening, $c_T = C_T/N_L$ is the trapped hydrogen concentration measured in hydrogen atoms per solvent atom, and the function $F(\varepsilon^p)$ describes the work hardening of the material as a function of the logarithmic plastic strain ε^p in uniaxial tension. Hydrogen is assumed not to change the work-hardening characteristics of the material. The yield stress σ_0 and function $F(\varepsilon^p)$ are determined from the measured uniaxial stress-strain curve of the 21-6-9 base material, which was assumed to reasonably represent the deformation response of austenite in the weld. Figure 7(c) shows the flow stress as a function of the plastic strain in the absence of hydrogen. The constitutive response of the materials was assumed to be rate independent with von Mises yielding and the associated flow rule. The relevant three-dimensional constitutive law can be found in the work of Sofronis et al.[33] It is noted that the adopted model of hydrogen-induced softening is just an attempt to account for the hydrogen's effect on dislocation mobility and is not an exhaustive description of the response of the material microstructure in the presence of hydrogen. The material parameters for the steel are listed in Table IV.

Table IV. Material Parameters Used in Simulation

| Properties	Symbol	Value
Young's modulus	E	196.6 GPa
Poisson's ratio	v	0.3
Initial yield stress in the absence of hydrogen	σ_0	485 MPa
Number of sites per trap[34,37]	α	10
Number of NILS per host atom	β	1
Trap binding energy[38]	E_B	9.65 kJ/mol (0.1 eV)
Molar volume of the host lattice	V_M	7.116×10^{-6} m³/mol
Partial molar volume of H[1]	V_H	2×10^{-6} m³/mol
Diffusion coefficient at temperature of 298 K[13]	D	1.9×10^{-16} m²/s
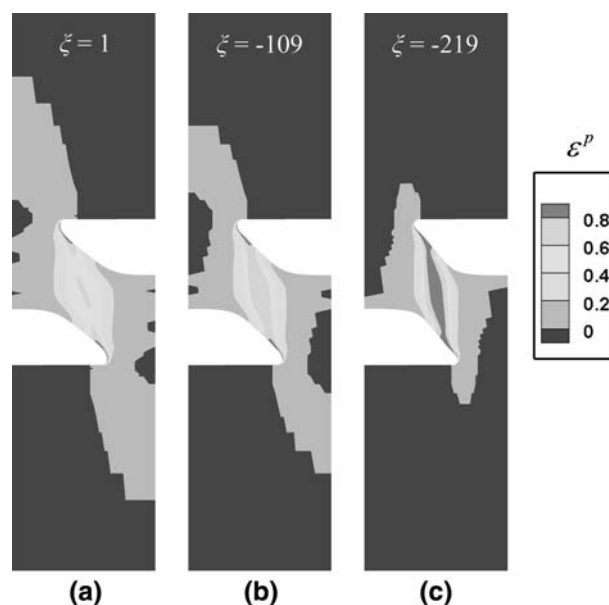
Fig. 8—Contour plots of equivalent plastic strain at time $t = 2$ min (macroscopic tensile strain of 10 pct) for various values of the hydrogen-induced softening parameter: $\xi = $ (a) 1 (no softening), (b) −109 (maximum softening of 20 pct), and (c) −219 (maximum softening of 40 pct).

The trapped hydrogen concentration and the effect of hydrogen on the plastic strain were investigated for several values of the softening parameter ξ. Contour plots of the effective plastic strain at the time of fracture initiation ($t = 2$ minutes) in the CT specimen are shown in Figure 8 for $\xi = 1$, −109, and −219. The value $\xi = 1$ corresponds to the absence of material softening, whereas the values −109 and −219 are associated with the 20 and 40 pct maximum hydrogen-induced reduction of the yield stress of the material at the hydrogen concentration in trapping sites $C_T = 1.5395 \times 10^{26}$ H/m³ ($c_T = 0.18$ at. pct), respectively. This concentration was derived at the location of the maximum trap density and in equilibrium with the NILS hydrogen at concentration $C_0 = 1.1003 \times 10^{27}$ H/m³ (or $c_0 = 1.3$ at. pct), i.e., potentially the largest trapping site concentration that could be attained in the domain.

Figure 8 shows the opening of the microcracks at $t = 2$ minutes, because large strain analysis was employed to monitor geometry changes upon loading. The corresponding results for the normalized hydrogen concentration at NILS, C_L/C_0, and traps (dislocations), C_T/C_0, are shown in Figures 9 and 10, respectively.

The calculations show that the plastic flow in the domain is concentrated in the region between the microcracks (Figure 8), with the rest of the material experiencing mainly elastic straining. Most important, the finite-element results demonstrate that accounting for hydrogen-induced localized softening leads to macroscopic intense shear deformation in the ligament between the microcracks. In the absence of localized softening, the plastic zone is very diffuse and spread throughout the ligament between the microcracks (Figure 8(a)). On the other hand, Figures 8(b) and (c) show that intense shear tends to localize in a band that becomes narrower as the softening effect of hydrogen becomes stronger. Upon straining, hydrostatic stress gradients bring about hydrogen diffusion through NILS, while dislocations generated in the plastically deformed regions constitute hydrogen trapping sites. In view of its low diffusivity in austenite, hydrogen diffused over extremely short distances during the time of straining (2 minutes) and, as a result, only minor spatial changes in the total hydrogen concentration $C_L + C_T$ occurred. However, intense plastic straining in the ligament between the microcracks causes hydrogen to be transferred locally from NILS to dislocation trapping sites and this accentuates the degree of the material softening, which, in turn, further intensifies the deformation. Figures 9 and 10 show that C_L/C_0 decreases while C_T/C_0 increases, indicating that NILS hydrogen populations in the ligament between the microcracks migrate to the dislocations generated locally by plastic straining. It is noted that intense shear deformation was also observed by Liang et al.[34] at a void surface, due to gradients in the plastic strain and the associated hydrogen concentration close to the void surface. In both the Liang et al. study[34] and the current study, intense shear deformation was ultimately caused by a gradient in the local flow stress that was associated with a nonuniform distribution of hydrogen.

While the simulations demonstrate that hydrogen-induced plastic softening can promote intense shear deformation in the ligaments, it is recognized that microcracking alone can potentially alter the stress state at a crack tip and affect shear localization. It is well known that plastic flow localization is strongly affected by hydrostatic constraint. For example, localization in uniaxial tension is easier under plane strain conditions than under axisymmetric conditions due to a higher constraint in the former case.[35] In the present work, the analysis of intense shear deformation between the microcracks was carried out in a unit cell simulating constraint uniaxial tension, as shown in Figure 7(b). This specific choice of the domain was prompted by the geometry of the microcracked region ahead of the main crack. In the absence of hydrogen, the incrementally loaded unit cell experienced a constraint the magnitude of which, as measured by the triaxiality $T = \Sigma_{kk}/3\Sigma_e$, was equal to 2.02 at the moment of macroscopic crack advance. Here, the parameter Σ_{kk} denotes the sum of the average macroscopic normal stresses acting on the cell boundaries and Σ_e denotes the Mises effective stress
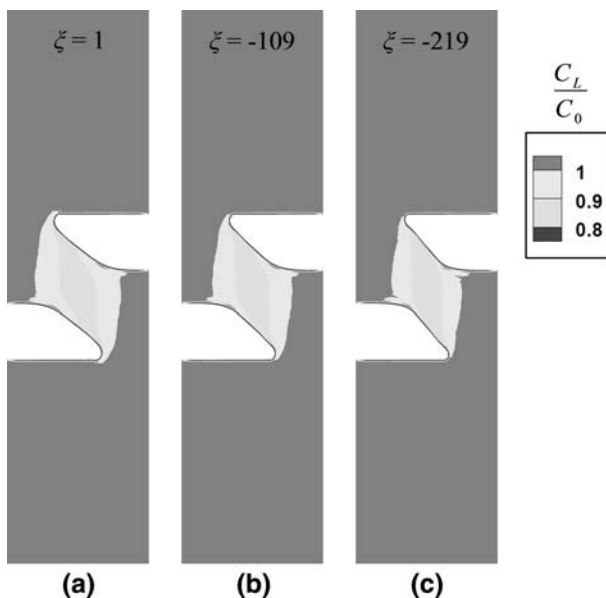

Fig. 9—Contour plots of normalized NILS hydrogen concentration, C_L/C_0, at macroscopic tensile strain 10 pct after 2 min from the start of loading and various values of the hydrogen-induced softening parameter: $\xi = $ (a) 1 (no softening), (b) −109 (maximum softening of 20 pct), and (c) −219 (maximum softening of 40 pct). The parameter $C_0 = 1.1003 \times 10^{27}$ H/m^3 (or $c_0 = 1.3$ at. pct) is the initial NILS hydrogen concentration.
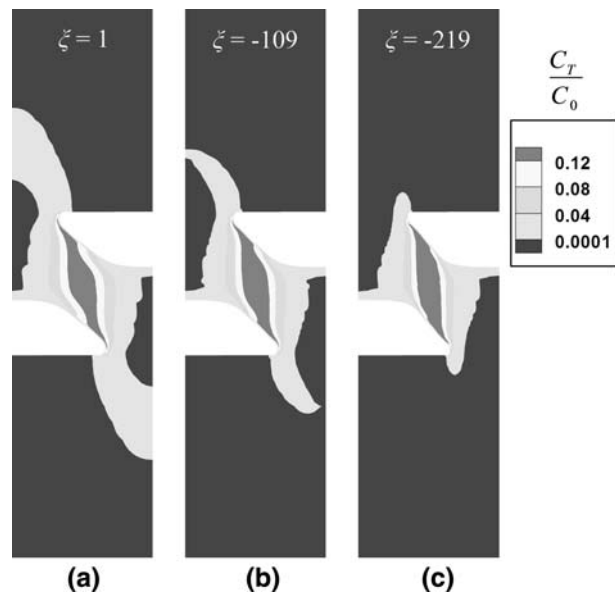

Fig. 10—Contour plots of normalized trapped hydrogen concentration, C_T/C_0, at macroscopic tensile strain 10 pct after 2 min from the start of loading and various values of the hydrogen-induced softening parameter: $\xi = $ (a) 1 (no softening), (b) −109 (maximum softening of 20 pct), and (c) −219 (maximum softening of 40 pct).

associated with those stresses. Therefore, in the absence of hydrogen, the simulation of the development of intense shear deformation between the microcracks took place under a triaxiality that is less than the triaxiality ($T = 2.7$) the material at the same location ahead of a blunting crack tip experiences in the absence of microcracking.[36] In other words, the fact that the presence of the microcracks relaxes the macroscopic constraint ahead of a crack tip is addressed by the model through the choice of the simulation domain and the associated boundary conditions. Of course, the precise magnitude of this relaxation and, hence, the applied hydrostatic constraint under which the calculation ought to have been carried out could have been found by solving directly the elastoplastic boundary value problem in the neighborhood of the main crack in the presence of the microcracks. That would be a more computationally demanding task and, certainly, the overall result would not be qualitatively different from that which the present unit cell approach furnishes. In the presence of hydrogen-induced softening, the constraint the unit cell experiences at the moment of macroscopic crack advance reduces even further. It is $T = 1.72$ with 20 pct softening and $T = 1.56$ with 40 pct softening. In fact, the main simulation result, that hydrogen causes intense shear deformation between the microcracks, as shown in Figure 8(c), is associated with a triaxiality of $T = 1.56$. In summary, the simulations were carried out under moderate triaxiality levels relative to the maximum triaxiality ahead of a crack tip in a nonmicrocracked material. The interesting point is that, despite this relatively relaxed macroscopic triaxiality, the simulations show that hydrogen can promote intense shear deformation through the gradient in the local flow stress it induces in the region between the microcracks.

The finite-element modeling was conducted to provide insight into the mechanism for microcrack linking during hydrogen-assisted crack propagation in 21-6-9/21-6-9 GTA welds. The microscopy results (*e.g.*, Figures 6(c) and (d)) revealed key details on the role of intense shear deformation, but microscopy evidence alone is unlikely to establish whether the intense shear deformation was enhanced by hydrogen. In the absence of physical evidence, the finite-element model results support the notion that hydrogen can facilitate the development of intense shear deformation between microcracks. While the finite-element model results are compelling, particularly because the model is based on the well-established physics of hydrogen-dislocation interactions, important model parameters have not been quantified for stainless steels. For example, the values for ξ (*i.e.*, -109 and -219) used in the flow rule were based on assumed magnitudes of hydrogen-induced local softening. The finite-element model could be a much more effective tool in providing mechanistic insight if the model parameters could be quantified with more certainty. Experimental studies of thermally activated dislocation motion could enable the development of flow rules for hydrogen-exposed materials. For example, properties such as the activation enthalpy for dislocation motion could be determined from stress relaxation tests on hydrogen-precharged specimens. Enhanced confidence in the flow rule for hydrogen-precharged stainless steels would be a consequential advancement for using finite-element models as tools in understanding hydrogen-assisted fracture.

V. CONCLUSIONS

The following conclusions are drawn from this study.

1. The fracture toughness of 21-6-9/21-6-9 GTA welds was severely degraded by 230 wppm (1.3 at. pct) of precharged hydrogen. The fracture initiation toughness and slope of the crack growth resistance curve for the hydrogen-precharged weld were reduced up to 60 and 90 pct, respectively, relative to the noncharged weld.
2. Hydrogen induced a change in the fracture mode, from microvoid coalescence in the noncharged weld to fracture associated with the dendritic microstructure in the hydrogen-precharged weld.
3. Hydrogen-assisted crack propagation in the weld proceeded by a sequence of microcrack formation at the weld ferrite, intense shear deformation in the ligaments separating microcracks, and then fracture of the ligaments.
4. One salient role of hydrogen in the crack propagation process was promoting microcrack formation at the austenite/ferrite interfaces and within the ferrite. In addition, hydrogen may have facilitated intense shear deformation in the ligaments separating microcracks. The intense shear deformation could be related to the development of a nonuniform distribution of hydrogen trapped at dislocations between microcracks, which, in turn, created a gradient in the local flow stress.

REFERENCES

1. N.R. Moody, S.L. Robinson, and W.M. Garrison: *Res. Mech.*, 1990, vol. 30, pp. 143–206.
2. H.G. Nelson: in *Treatise on Materials Science and Technology: Embrittlement of Engineering Alloys*, C.L. Briant and S.K. Banerji, eds., Academic Press, New York, NY, 1983, vol. 25, pp. 275–359.
3. A.W. Thompson and I.M. Bernstein: in *Advances in Corrosion Science and Technology*, M.G. Fontana and R.W. Staehle, eds., Plenum Press, New York, NY, 1980, vol. 7, pp. 53–175.
4. G.R. Caskey: in *Hydrogen Degradation of Ferrous Alloys*, R.A. Oriani, J.P. Hirth, and M. Smialowski, eds., Noyes Publications, Park Ridge, NJ, 1985, pp. 822–62.
5. J.A. Brooks and A.W. Thompson: *Int. Mater. Rev.*, 1991, vol. 36, pp. 16–44.
6. J.A. Brooks and A.J. West: *Metall. Trans. A*, 1981, vol. 12A, pp. 213–23.

7. J.A. Brooks, A.J. West, and A.W. Thompson: *Metall. Trans. A*, 1983, vol. 14A, pp. 75–84.

8. M.I. Luppo, A. Hazarabedian, and J. Ovejero-Garcia: *Corros. Sci.*, 1999, vol. 41, pp. 87–103.

9. M.J. Morgan, G.K. Chapman, M.H. Tosten, and S.L. West: *Trends in Welding Research: Proc. 7th Int. Conf.*, ASM INTERNATIONAL, Materials Park, OH, 2006, pp. 743–48.

10. A.M. Nasreldin, M.M.A. Gad, I.T. Hassan, M.M. Ghoneim, and A.A. El-Sayed: *J. Mater. Sci. Technol.*, 2001, vol. 17, pp. 444–48.

11. C. Pan, Y.J. Su, W.Y. Chu, Z.B. Li, D.T. Liang, and L.J. Qiao: *Corros. Sci.*, 2002, vol. 44, pp. 1983–93.

12. *Annual Book of ASTM Standards*, ASTM International, West Conshohocken, PA, 1997, vol. 03.01, pp. 968–91.

13. C. SanMarchi, B.P. Somerday, and S.L. Robinson: *Int. J. Hydrogen Energy*, 2007, vol. 32, pp. 100–16.

14. K.A. Nibur, B.P. Somerday, D.K. Balch, and C. SanMarchi: *Acta Mater.*, 2009, vol. 57, pp. 3795–3809.

15. D.J. Kotecki and T.A. Siewert: *Weld. J.*, 1992, vol. 71, pp. 171s–178s.

16. C. SanMarchi, B.P. Somerday, J. Zelinski, X. Tang, and G.H. Schiroky: *Metall. Mater. Trans. A*, 2007, vol. 38A, pp. 2763–75.

17. H.K. Birnbaum and P. Sofronis: *Mater. Sci. Eng.*, 1994, vol. A176, pp. 191–202.

18. M. Menard, J.M. Olive, A.-M. Brass, and I. Aubert: in *Environment-Induced Cracking of Materials: Chemistry, Mechanics and Mechanisms*, S.A. Shipilov, R.H. Jones, J.-M. Olive, and R.B. Rebak, eds., Elsevier, Oxford, United Kingdom, 2008, vol. 1, pp. 179–88.

19. K.A. Nibur, D.F. Bahr, and B.P. Somerday: *Acta Mater.*, 2006, vol. 54, pp. 2677–84.

20. I.M. Robertson: *Eng. Fract. Mech.*, 2001, vol. 68, pp. 671–92.

21. C. SanMarchi, K.A. Nibur, D.K. Balch, and B.P. Somerday: *J. Pressure Vessel Technol.*, 2008, vol. 130, art. no. 041401, 9 pp.

22. J.P. Hirth: in *Hydrogen Effects on Material Behavior*, N.R. Moody and A.W. Thompson, eds., TMS, Warrendale, PA, 1990, pp. 677–85.

23. J.P. Hirth: in *Hydrogen Effects in Materials*, A.W. Thompson and N.R. Moody, eds., TMS, Warrendale, PA, 1996, pp. 507–22.

24. P. Sofronis and H.K. Birnbaum: *J. Mech. Phys. Solids*, 1995, vol. 43, pp. 49–90.

25. Y. Liang, P. Sofronis, and N. Aravas: *Acta Mater.*, 2003, vol. 51, pp. 2717–30.

26. P. Sofronis and R.M. McMeeking: *J. Mech. Phys. Solids*, 1989, vol. 37, pp. 317–50.

27. Y. Liang and P. Sofronis: *Modell. Simul. Mater. Sci. Eng.*, 2003, vol. 11, pp. 523–51.

28. H. Peisl: in *Topics in Applied Physics: Hydrogen in Metals I*, G. Alefeld and J. Volkl, eds., Springer-Verlag, New York, NY, 1978, vol. 28, pp. 53–74.

29. R.A. Oriani: *Acta Metall.*, 1970, vol. 18, pp. 147–57.

30. R.B. McLellan: *Acta Metall.*, 1979, vol. 27, pp. 1655–63.

31. J.K. Tien, A.W. Thompson, I.M. Bernstein, and R.J. Richards: *Metall. Trans. A*, 1976, vol. 7A, pp. 821–29.

32. J.J. Gilman: *Micromechanics of Flow in Solids*, McGraw-Hill, New York, NY, 1969.

33. P. Sofronis, Y. Liang, and N. Aravas: *Eur. J. Mech., A/Solids*, 2001, vol. 20, pp. 857–72.

34. Y. Liang, P. Sofronis, D.C. Ahn, R. Dodds, and D. Bammann: *Mech. Mater.*, 2008, vol. 40, pp. 115–32.

35. J.R. Rice: *Proc. 14th Int. Congr. on Theoretical and Applied Mechanics*, North-Holland Publishing, Delft, The Netherlands, 1977, pp. 207–20.

36. D.C. Ahn, P. Sofronis, and R.H. Dodds: *Int. J. Fract.*, 2007, vol. 145, pp. 135–57.

37. J.P. Hirth and B. Carnahan: *Acta Metall.*, 1978, vol. 26, pp. 1795–1803.

38. G.J. Thomas: in *Hydrogen Effects in Metals*, I.M. Bernstein and A.W. Thompson, eds., TMS-AIME, Warrendale, PA, 1981, pp. 77–84.